Analysis and Characterization of Photon-Photon Resonance in Coupled Dual-Element Photonic Crystal Vertical Cavity Surface Emitting Laser Arrays

William North, *Member, IEEE*, Nusrat Jahan, *Member, IEEE*, Pawel Strzebonski, *Member, IEEE*, Arjun Khurana, *Member, IEEE*, Stephen E. Ralph, *Senior Member, IEEE*, and Kent D. Choquette, *Fellow, IEEE*

***Abstract*—We report a photonic resonance at the frequency difference between non-degenerate modes of dual-element photonic crystal vertical cavity surface emitting laser arrays. The evolution of modes in coupled dual-element laser arrays biased in the coherently coupled region is examined through theory and experimentation. A complex waveguide simulation predicts two supermodes for operation along the coherently coupled region which results in increased output power, visibility, and a photon-photon resonance frequency above the carrier-photon resonance frequency. Experimental analysis of number of spectral peaks, far-field beam profile, spectral linewidth, and noise frequency response along the coherently coupled region as a function of input current shows that the two supermodes must lase simultaneously within the coherently coupled region. The two supermodes are nearly degenerate and the resulting beating between the supermodes creates a photon-photon resonance. For the nominally 850 nm arrays characterized, we identify the photon-photon resonance at approximately 20 GHz for operation along the coherently coupled region.**

***Index Terms*—Optical coupling, phased arrays, semiconductor laser arrays, vertical cavity surface emitting lasers.**

I. Introduction

DIRECTLY modulated lasers are attractive for data centers and other short-distance optical communication systems due to their low power consumption and size. These advantages are realized because the generation and modulation of light occur in the same region. However, modulation rates for these lasers are limited by the carrier-photon resonance (CPR) or relaxation oscillation frequency, which arises from the interaction between injected electrons and emitted photons. To address this challenge, researchers have explored less conventional designs to extend the modulation bandwidth such as using detuned loading [1], in-cavity frequency modulation–amplitude modulation conversion [2], and modulation sidebands to form a photon-photon resonance (PPR) [3].

Traditionally applied to semiconductor edge-emitting lasers, vertical cavity surface emitting lasers (VCSEL) could also benefit from similar techniques to extend their modulation bandwidth. Conventional VCSELs likely have an achievable bandwidth limited to around 25 GHz due to thermal effects and electrical parasitics [4]. Several mechanisms to extend the bandwidth have been pursued such as coupled cavities [5], injection locking [6], VCSEL mini-arrays [7], and using optical coupling to create a photon-photon resonance (PPR) [8].

Optical coupling enhances the modulation bandwidth by introducing mode beating. This occurs when two modes of the laser resonate at slightly different frequencies creating a PPR at a frequency higher than the CPR. Thus, the PPR adds higher frequency components to extend the laser modulation bandwidth beyond what the CPR by itself can provide. Recent demonstrations have claimed to use a PPR to extend modulation bandwidth. For example, the bow-tie VCSELs [8] and coherently coupled VCSEL arrays [9], [10], [11] have been shown to extend the modulation bandwidth beyond conventional VCSEL limits, although without direct evidence of a PPR.

We report the prediction and characterization of a PPR through theory and experimentation on coupled dual-element photonic crystal VCSEL arrays [10]. First, we review the models used to describe VCSEL array operation and highlight the resulting predictions. A significant outcome of our analysis is the prediction of two non-degenerate supermodes when the array is operated in the coherently coupled regime. Then, we validate the predictions by analyzing experimental data, such as far-field beam profiles, spectral data, and noise spectrums measured with the left and right element at fixed currents. Finally, we explain how the PPR arises from two nearly degenerate supermodes beating against each other, and how this opens up opportunities for engineering the frequency and strength of the PPR for enhancement of the direct modulation rate of the VCSEL array.

Manuscript received 26 May 2023; revised 6 July 2023; accepted 27 July 2023. Date of publication 23 August 2023; date of current version 2 January 2024. This work was supported in part by the funding by U.S. Navy under Award N6833522C0229. *(Corresponding author: William North.)*

William North, Nusrat Jahan, and Kent D. Choquette are with the Department of Electrical and Computer Engineering, University of Illinois at Urbana-Champaign, Urbana, IL 61801 USA (e-mail: wnorth2@illinois.edu; nusratj2@illinois.edu; choquett@illinois.edu).

Pawel Strzebonski was with the University of Illinois at Urbana-Champaign, Urbana, IL 61801 USA. He is now with the Meta, Sunnyvale, CA 94089 USA (e-mail: pawelstrzebonski@gmail.com).

Arjun Khurana and Stephen E. Ralph are with the School of Electrical and Computer Engineering, Georgia Institute of Technology, Atlanta, GA 30332 USA (e-mail: akhurana9@gatech.edu; stephen.ralph@ece.gatech.edu).

Color versions of one or more figures in this article are available at https://doi.org/10.1109/JLT.2023.3300969.

Digital Object Identifier 10.1109/JLT.2023.3300969

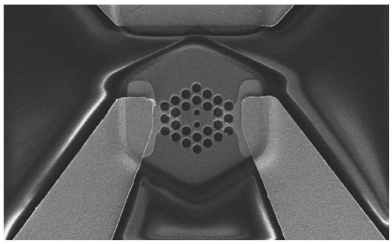

Fig. 1. Scanning electron micrograph image of dual-element photonic crystal VCSEL array defined by two missing holes in the photonic crystal pattern [9].

II. Theory

A coupled dual-element photonic crystal VCSEL array operating in its coherently coupled regime has demonstrated unique static and dynamic properties such as increased optical power [12], beam-steering [13], increased small-signal modulation bandwidth [9], enhanced digital modulation rate [14], and reduced noise and harmonic distortions [12]. These devices incorporate a photonic crystal pattern etched into the top mirror to enable single-mode behavior in each cavity, with ion implantation providing electrical isolation between cavities [10]. The photonic crystal has two defects, as shown in Fig. 1, that roughly correspond to the gain apertures of the left and right element. The photonic crystal hole diameters are 2.4 μm, and the pitch between holes is 4 μm in a hexagonal pattern. The cavities are formed by a missing hole, where the 6.6 μm cavity diameter is measured from the inner edges of the six holes surrounding each cavity. The photonic crystal holes between the cavities have a reduced diameter to promote optical coupling [15]. The photonic crystal holes are etched into the top distributed Bragg reflector. These devices emit light at a wavelength of 850 nm.

Chronologically, theoretical work on coupled dual-element photonic crystal VCSEL arrays first focused on defining the refractive index profile by using a coupling coefficient with coupled mode theory [16] and coupled rate equations [17]. This was followed by the use of complex waveguide (CWG) simulations [18] using the finite difference method. Most recently, a time-varying confinement factor with coupled rate equations has been utilized [19]. These methods complement each other with recent work identifying the connections between the approaches [19]. In this section, we review the theoretical results common to these models, all of which point to the simultaneous lasing of two nearly degenerate modes in the coherently coupled regime.

The refractive index profile serves as the foundation of the coupled dual-element photonic crystal VCSEL. The index of the left and right element can be tuned through an independent injection current to the cavities [20]. When carriers are injected, the index profile changes through thermal heating and electronic suppression, and because the ion implantation precludes free carriers suppressing the index between the cavities, an anti-guided waveguide arises [21]. When the waveguide core index is not symmetric, which corresponds to combinations of unequal current injection into the two cavities above threshold, two local modes exist confined separately to their own cavity and act as independent VCSELs [22]. However, as the waveguide becomes symmetric, two nearly degenerate modes manifest

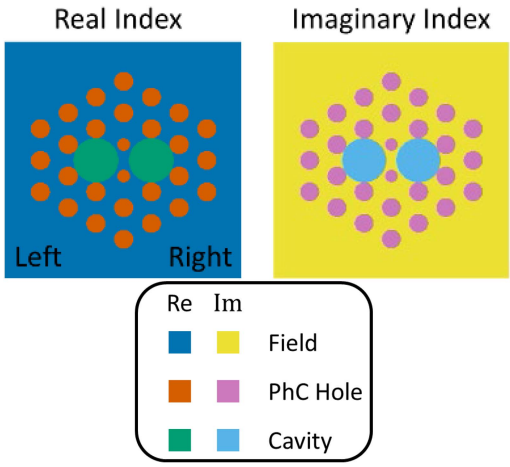

Fig. 2. Complex refractive index profile used for the complex waveguide model. The corresponding parameters are shown in Table I.

across the cavities which are known as supermodes [22]. The injection current where the supermodes exist is referred to as the coherently coupled regime and corresponds to roughly equal current injection into each element above threshold.

A complex coupling coefficient model provides a mechanism to connect the mode fields shared across the cavities. The real part of the coupling coefficient describes the rate of energy transfer between cavities, and the imaginary part describes the energy loss as it flows between cavities as a measure of the gain separation between the two cavities and determines the relative gain-loss contrast between the supermodes [17]. Considering only a real coupling coefficient, the overall system is Hermitian and allows modes in two configurations: the first has the same phase in each cavity (referred to as in-phase), while the other has a π phase difference between cavities (referred to as out-of-phase) [23]. When including the imaginary part of the coupling coefficient, coupled rate equations predict a lower threshold for coherently coupled modes then the localized modes, resulting in a power enhancement along the coherently coupled region [17]. This also allows for the phase between cavities to change and modifies the in-phase and out-of-phase modes away from their Hermitian profile [24]. The two supermodes are distinguishable from each other except at the exceptional point where the phase difference is $\pi/2$ [25]. However, current injection is not clearly linked with modal properties in these models.

Therefore, we extend our analysis using a two-dimensional CWG simulation that accounts mode evolution with changing index suppression between the cavities arising from current injection. The simulation calculates the effective index for each mode based on the refractive index profile of the array, as shown in Fig. 2, with parameters listed in Table I. Using this complex index profile, we solved for the effective indices of the lasing modes as a function of the confinement factor for each mode [18], [26]. The real effective index is proportional to the mode wavelength, and the imaginary part is related to the modal gain. Though the waveguide generally supports two modes, the supermodes arise when the refractive index profile is nearly symmetric (i.e., with nearly equal current injection), exhibiting nearly degenerate effective complex refractive indexes and nearly equal

TABLE I
COMPLEX WAVEGUIDE SIMULATION PARAMETERS

Parameter	Value
Field Refractive Index	$3.451 + (15 \times 10^{-4})i$
Cavity Refractive Index	$3.449 + \Delta n_{elect} - (3 \times 10^{-3})i$
Photonic Crystal Hole Index	$2 + 0i$

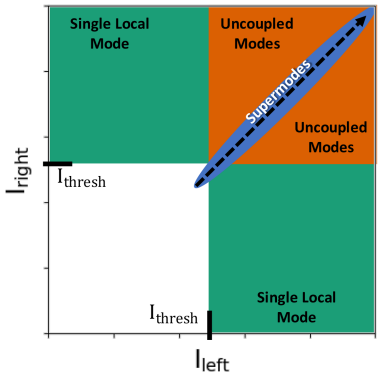

Fig. 3. Sketch of the three mode regimes for coupled dual-element photonic crystal VCSEL arrays: single local mode (green), dual supermodes (blue), and dual uncoupled modes (orange). The dashed black arrow inside the supermodes regime corresponds to approximately equal current injection into the cavities and is referred to as the coherently coupled ridge.

confinement factors [18]. As the waveguide becomes anti-symmetrical, the spectral splitting between the modes increases, and the modes tend to localize to one cavity [22].

Based on this analysis, we identify three operating regions shown in Fig. 3: a region where one element has a single local mode (green), a supermode region demonstrating strong interference between supermodes and a nearly degenerate spectral mode (blue), and a transition region with weak interference and two spectral modes (orange). The dashed black arrow in Fig. 3 indicates the coherently coupled "ridge", where the refractive index is nearly symmetric and approximately equal current injected into each element above threshold.

To analyze the modal behavior along the coherently coupled ridge or the black arrow in Fig. 3, we limit the CWG simulation to a symmetric refractive index profile and increasing index suppression, Δn_{elect}, to represent equally increasing current into both cavities. This allowed us to examine the difference between supermodes in the real index, which is proportional to the frequency separation, and the difference in the imaginary index, which is related to gain separation. The simulation used the parameters in Table I and increasing index suppression from increasing current is indicated by the black dashed arrow in Fig. 3. In comparison to the VCSEL parameters used in [22], we increased the imaginary part of the field index to 15×10^{-4}, reduced the imaginary part of the core index to 3×10^{-4}, and lowered the real part of the real index in the cavity following [19]. These modified values are consistent with values derived from typical 850 nm VCSELs [27]. The results of this simulation are shown in Fig. 4 where the horizontal axis is the index suppression along the coherently coupled ridge, the left vertical axis is the

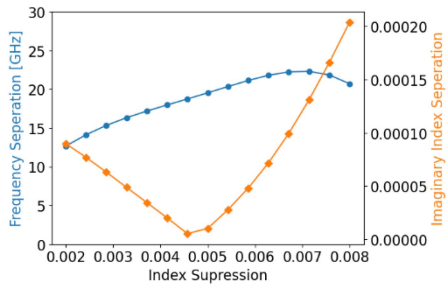

Fig. 4. Spectral splitting (blue circles) and imaginary index separation (orange diamonds) as a function of changing the refractive index suppression while keeping the index profile symmetric nominally from threshold (left) to rollover (right). The increase in index suppression follows the same line as the black arrow in Fig. 3.

frequency separation between supermodes, and the right vertical axis is the imaginary index separation.

One can make predictions about the far-field beam characteristics observed under coherently coupled array operation along the coherently coupled ridge since the imaginary index separation plotted in Fig. 4 is proportional to the mode suppression ratio [22]. When the array is operated at imaginary index suppression values less than where the imaginary index splitting is zero, which occurs near an index suppression of 0.0045, the out-of-phase supermode dominates the far-field beam profile. Conversely, when operated at a greater imaginary index suppression, the far-field beam profile switches and the in-phase supermode dominates [28]. Interestingly, when the imaginary index separation is zero, which occurs at an index suppression of 0.0065, the equal gain implies equal contributions from both supermodes resulting in a Gaussian-like far-field beam profile. Moreover, we can do the reverse and find the mode suppression ratio from the far-field beam profile by calculating the Fourier transform of the far-field beam profile [29].

Finally, we observe that there is always some separation between the real index of the supermodes. This implies a small yet significant spectral separation between modes. When using a time-varying confinement factor with coupled rate equations, a beating between modes is predicted to occur, with its strength depending on the overlap between modes, the mode suppression ratio between supermodes, and the asymmetry of the array structure [19]. This beating between supermodes results in a PPR at the frequency difference estimated in Fig. 4. Such a PPR is predicted to enhance the small-signal modulation response [19] and is the reason for the high modulation rates demonstrated in VCSEL arrays [14].

III. EXPERIMENT

The spectra, far-field beam profiles, and noise spectra of coupled dual-element photonic crystal VCSEL arrays are characterized at room temperature with direct current input and continuous wave operation of the laser array. To highlight the location of coherently coupled operation, Fig. 5 presents the number of spectral peaks observed using an optical spectrum analyzer versus injection current, where the axes represent the

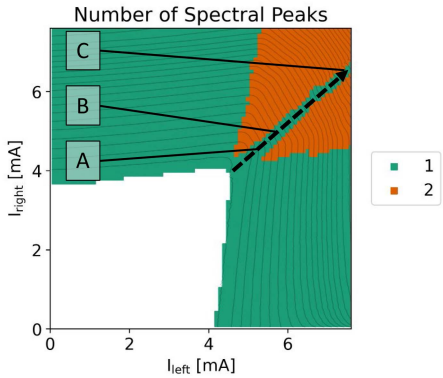

Fig. 5. Number of spectral peaks versus injection current for a coupled dual-element photonic crystal VCSEL array. The green region occurring where I_{left} and I_{right} are approximately equal (shown as a black arrow) represents the coherently coupled ridge.

current injection to the left and right element and the green and orange colors represent one and two spectral peaks respectively. Comparing this figure to Fig. 3, we observe that the top left and bottom right green sections correspond to the single local modes, the orange regions correspond to the uncoupled local cavity modes, and the center green section, where I_{left} and I_{right} are approximately equal corresponds to the supermode coherently coupled region. The black arrow represents the coherently coupled ridge, and we limit subsequent experimental collections to current pairs along the coherently coupled ridge, which in Fig. 5 corresponds to I_{left} current varying from threshold at 4.5 mA to rollover at 7.5 mA. The points A-C corresponds to Fig. 6(a)–(c) respectively.

In Fig. 6, we plot representative far-field beam profiles measured at different injection currents along the coherently coupled ridge with an inset showing the calculated visibility and mode suppression ratio. We calculate the visibility from Fourier transform and the mode suppression ratio from $MSR = \frac{1+V}{1-V}$ where V is visibility [29]. Fig. 6(a) shows the far-field beam profile where the out-of-phase supermode dominates at low currents, Fig. 6(b) shows where both supermodes have nearly identical intensity and the far-field beam profile is Gaussian-like, and Fig. 6(c) is at higher injection currents where the in-phase supermode dominates. The far-field beam profiles in Fig. 6(a)–(c) correspond to the points A-C indicated in Figs. 7 and 8. The supermode evolution with increasing current is consistent with [30] and our simulations shown in Fig. 4.

Next, we plot the visibility of the far-field beam profile and mode suppression ratio as a function of the I_{left} current from threshold to rollover along the coherently coupled ridge (I_{right} values are omitted for clarity but are approximately equal to I_{left}) in Fig. 7. These figures demonstrate a clear correlation between the predicted visibility and mode suppression ratio that arises from the imaginary index separation in the CWG simulations from Fig. 3. Additionally, we identify key operation points along the coherently coupled ridge: A is where the out-of-phase supermode is dominate, B represents where the two supermodes have nearly identical gain, and C is where the in-phase supermode

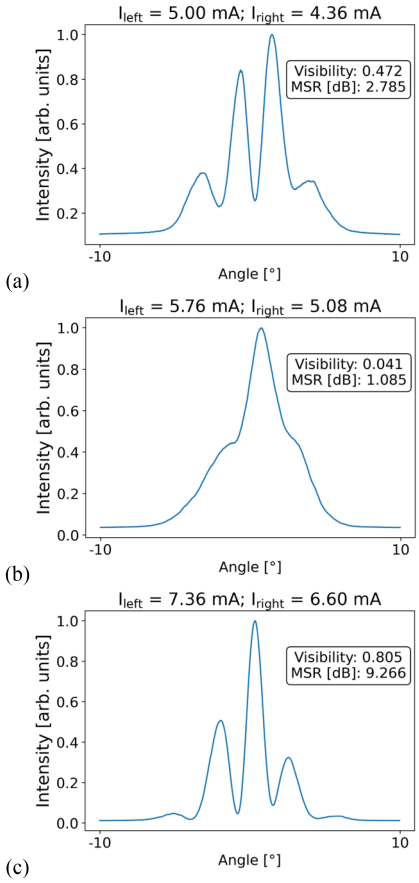

Fig. 6. Selected far-field beam profiles along the coherently coupled ridge where (a) the out-of-phase supermode dominates, (b) both supermodes have nearly identical intensities, and (c) the in-phase supermode dominates. The profiles are collected at point indicated in Figs. 7 and 8.

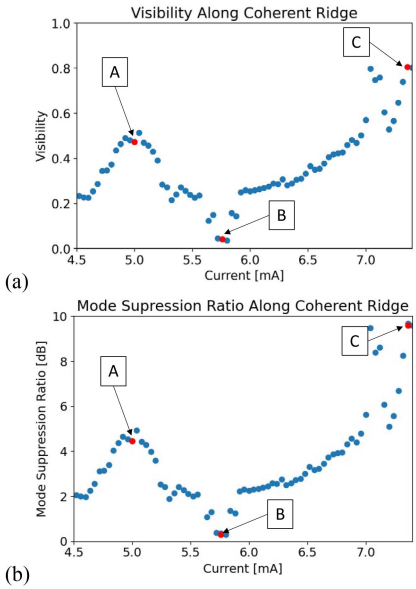

Fig. 7. (a) Calculated far-field visibility and (b) mode suppression ratio as a function of the I_{left} current from threshold to rollover along the coherently coupled ridge (I_{right} values are omitted for succinctness). Points A-C correspond to Fig. 6(a)–(c) respectively.

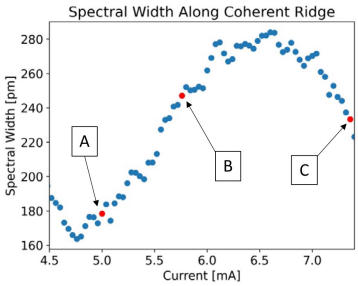

Fig. 8. Spectral width as a function of the I_{left} current from threshold to rollover along the coherently coupled ridge (I_{right} values are omitted for succinctness). Points A-C correspond to Fig. 6(a)–(c) respectively.

dominates. These points correspond to far-field beam profiles in Fig. 6(a)–(c) respectively.

Though we observed a single lasing spectral peak along the coherently coupled ridge in Fig. 5, the single spectral peaks exhibit varying linewidths. In Fig. 8, we measured the spectral linewidth 10 dB below the maximum along the coherently coupled ridge, where a larger linewidth presumably correlates to a greater frequency separation. The points A, B, and C represent array operation when the out-of-phase mode dominates, when the modes have nearly equal gain, and when the in-phase mode dominates and correspond to Fig. 6(a)–(c) respectively. We find qualitative agreement between the measured linewidths in Fig. 8 and the predicted frequency separation trend in Fig. 4.

To obtain the PPR frequency, we analyze the noise spectrum along the coherently coupled ridge [11]. This measurement involves setting left and right currents to fixed current values along the coherently coupled ridge, directing light to a photoreceiver, and measuring the average noise level, normalized to a 1 Hz noise power bandwidth, using an electrical spectrum analyzer. We first capture the dark noise by measuring the noise level with only the photoreceiver on. Next, we turn on the VCSEL array and capture the noise spectrum and subtract the dark noise along the coherently coupled ridge. In Fig. 9(a), we plot the noise spectrum as a function of frequency while biasing the array just outside of the coherently coupled ridge with both elements lasing (i.e., orange region in Fig. 5) where the noise spectrum is similar to that of a conventional VCSEL, where the CPR frequency at this bias is around 5 GHz. In Fig. 9(b), we plot the noise spectrum at the middle on the coherently coupled ridge (I_{right} increased by 40 μA) and observe a second resonance peak at a frequency higher than the CPR frequency that only occurs within the coherently coupled region, which we identify as the PPR frequency at 20.8 GHz.

When we adjust the bias away from the coherently coupled ridge by increasing I_{right} and leaving I_{left} the same, we observe that the PPR tends towards higher frequencies as shown in Fig. 10. Specifically, as we increase I_{right} in 40 μA steps, the PPR frequency increases from 20.56 GHz to 21.0 GHz. This trend aligns with predictions from CWG simulations which suggested that the frequency separation increases as one biases away from the symmetric profile of the anti-guided waveguide[22].

As we increase the bias current in the device, the maximum response of the PPR peak can reach the same relative strength

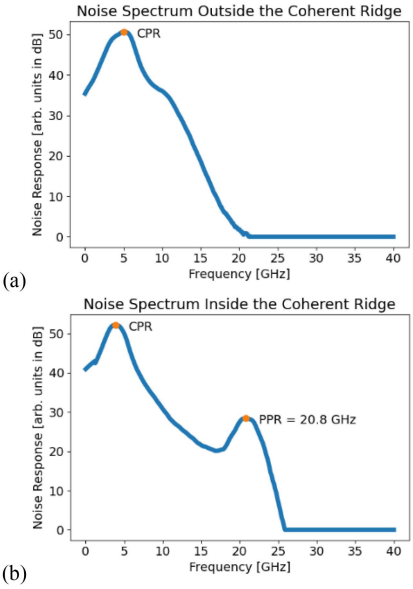

Fig. 9. Noise spectrum (a) outside of the coherently coupled region (I_{left} = 5.32 mA and I_{right} = 5.00 mA) and (b) inside the coherently coupled region (I_{left} = 5.32 mA and I_{right} = 4.60 mA). The lower frequency peak is attributed to the CPR and the higher frequency peak is attributed to the PPR.

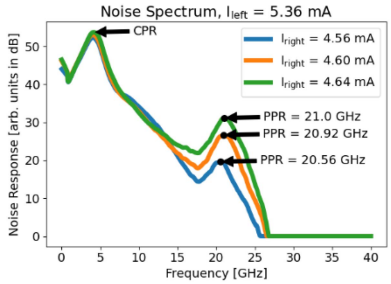

Fig. 10. Noise spectrums when moving away from the coherently coupled ridge. I_{left} remains the same while I_{right} increases in increments of 40 μA steps.

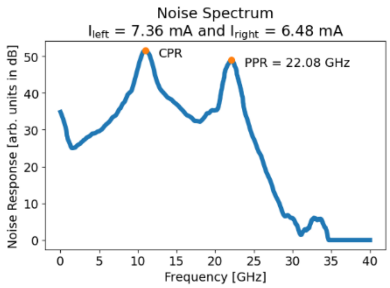

Fig. 11. Noise spectrum showing that the PPR peak response can nearly match the CPR peak response at high current pairs.

as the CPR peak as depicted in Fig. 11. This represents a 20 dB increase in strength from the noise spectrums observed near threshold as shown in Figs. 9 and 10. We attribute this higher PPR strength to the mode suppression ratio between supermodes as discussed in [19]. The PPRs in Figs. 10 and 11 demonstrate the added frequency components that provide the mechanism for enhanced modulation bandwidth of a dual-element VCSEL array over that of a conventional single element VCSEL.

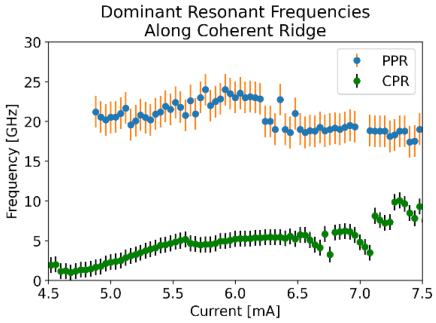

Fig. 12. Dominant resonant frequencies as a function of the I_{left} current from threshold to rollover along the coherently coupled ridge (I_{right} values are omitted for succinctness).

In Fig. 12, we measured the dominant resonant frequencies along the coherently coupled ridge. While acquiring these measurements, we encountered difficulty in precisely identifying the PPR peak frequency due to noise in the data sets. In contrast, the CPR was easier to identify. Therefore, we conservatively estimated an uncertainty of +/− 2 GHz for the PPR measurements and +/− 1 GHz for the CPR measurements. In Fig. 12, we omitted PPR frequencies below 4.8 mA near threshold because the PPR peak was not prominent. We observed that the PPR near threshold was around 20 GHz, increases to 23 GHz at 6.2 mA, approximately 1.4x threshold, and decreases to approximately 18 GHz at twice threshold. This trend has qualitative agreement with the frequency separation estimated from our CWG simulations shown in Fig. 4, where the PPR frequency variation is relatively small over a wide operating range.

IV. Conclusion

In this work, we established that an anti-guided waveguide, which supports two modes, is formed upon fixed current injection in the VCSEL array. When operated in the coherently coupled regime, where the left and right current injection is roughly equal, two nearly degenerate supermodes exist simultaneously. The beating between these two supermodes gives rise to the PPR, even if one supermode dominates over the other. We then measured the PPR along the coherently coupled ridge from threshold to rollover and showed that it has a narrow spectral width, a relatively unvarying frequency response over the device's operating range, has a strong response strength at high current pairs, and is the mechanism that is attributed to the demonstrated high modulation rates.

Since modulation bandwidth increases are critical for data communication applications, we must explore non-conventional means to enhance the VCSEL data rate. One approach is through optical coupling and the coupled dual-element photonic crystal VCSEL array. Both theoretical analysis and experimental data demonstrate that these VCSEL arrays possess unique properties that conventional VCSELs do not: namely the presence of the PPR. The PPR which occurs at higher frequency than the CPR can thus effectively increase the modulation bandwidth of the coupled-array over that of a single VCSEL. The potential for engineering the PPR frequency and strength is promising due to the device parameters that can be modified, such as the index profile, photonic crystal design, and asymmetric cavities, among others. Tailoring these parameters provides a promising tool towards engineering the PPR frequency and realizing future VCSEL modulation data rates of 100 Gbps [11].

Acknowledgment

The authors thank S. T. M. Fryslie, B. Thompson, M. T. Johnson, H. Dave, and K. Lakomy for their prior contributions to design, fabrication, and analysis of the photonic crystal VCSEL arrays.

References

[1] K. Vahala and A. Yariv, "Detuned loading in coupled cavity semiconductor lasers—Effect on quantum noise and dynamics," *Appl. Phys. Lett.*, vol. 45, no. 5, pp. 501–503, Sep. 1984, doi: 10.1063/1.95316.

[2] Y. Matsui, "3 directly modulated laser technology: Past, present, and future," in *Datacenter Connectivity Technologies: Principles and Practice*. Kolkata, West Bengal, India: River Publishers, 2017, pp. 87–172, Apr., 11, 2023. [Online]. Available: https://ieeexplore.ieee.org/abstract/document/9228174

[3] L. Bach, W. Kaiser, J. P. Reithmaier, A. Forchel, T. W. Berg, and B. Tromborg, "Enhanced direct-modulated bandwidth of 37 GHz by a multi-section laser with a coupled-cavity-injection-grating design," *Electron. Lett.*, vol. 39, no. 22, pp. 1592–1593, Oct. 2003, doi: 10.1049/el:20031018.

[4] A. Larsson, J. S. Gustavsson, A. Fülöp, E. Haglund, E. P. Haglund, and A. Kelkkanen, "The future of VCSELs: Dynamics and speed limitations," in *Proc. IEEE Photon. Conf.*, 2020, pp. 1–2. doi: 10.1109/IPC47351.2020.9252236.

[5] C. Chen and K. D. Choquette, "Analog and digital functionalities of composite-resonator vertical-cavity lasers," *J. Lightw. Technol.*, vol. 28, no. 7, pp. 1003–1010, Apr. 2010, doi: 10.1109/JLT.2010.2041747.

[6] M. Pflüger, D. Brunner, T. Heuser, J. A. Lott, S. Reitzenstein, and I. Fischer, "Injection locking and coupling the emitters of large VCSEL arrays via diffraction in an external cavity," *Opt. Exp., OE*, vol. 31, no. 5, pp. 8704–8713, Feb. 2023, doi: 10.1364/OE.473449.

[7] N. N. Ledentsov et al., "High speed VCSEL technology and applications," *J. Lightw. Technol.*, vol. 40, no. 6, pp. 1749–1763, Mar. 2022, doi: 10.1109/JLT.2022.3149372.

[8] H. Dalir and F. Koyama, "High-speed operation of bow-tie-shaped oxide aperture VCSELs with photon–photon resonance," *Appl. Phys. Exp.*, vol. 7, no. 2, Jan. 2014, Art. no. 022102, doi: 10.7567/APEX.7.022102.

[9] S. T. M. Fryslie, M. P. T. Siriani, D. F. Siriani, M. T. Johnson, and K. D. Choquette, "37-GHz modulation via resonance tuning in single-mode coherent vertical-cavity laser arrays," *IEEE Photon. Technol. Lett.*, vol. 27, no. 4, pp. 415–418, Feb. 2015, doi: 10.1109/LPT.2014.2376959.

[10] S. T. M. Fryslie et al., "Modulation of coherently coupled phased photonic crystal vertical cavity laser arrays," *IEEE J. Select. Topics Quantum Electron.*, vol. 23, no. 6, Nov. 2017, Art. no. 1700409, doi: 10.1109/JSTQE.2017.2699630.

[11] K. D. Choquette, S. E. Ralph, A. Melgar, N. Jahan, W. North, and J. A. Tatum, "Supermode dynamics for VCSEL modulation," in *Proc. IEEE Photon. Conf.*, 2021, pp. 1–2. doi: 10.1109/IPC48725.2021.9592985.

[12] H. Dave, Z. Gao, S. T. M. Fryslie, B. J. Thompson, and K. D. Choquette, "Static and dynamic properties of coherently-coupled photonic-crystal vertical-cavity surface-emitting laser arrays," *IEEE J. Select. Topics Quantum Electron.*, vol. 25, no. 6, Nov./Dec. 2019, Art. no. 1700208, doi: 10.1109/JSTQE.2019.2917551.

[13] M. T. Johnson, D. F. Siriani, M. P. Tan, and K. D. Choquette, "Beam steering via resonance detuning in coherently coupled vertical cavity laser arrays," *Appl. Phys. Lett.*, vol. 103, no. 20, Nov. 2013, Art. no. 201115, doi: 10.1063/1.4830432.

[14] H. Dave et al., "Digital modulation of coherently-coupled 2x1 vertical-cavity surface-emitting laser arrays," *IEEE Photon. Technol. Lett.*, vol. 31, no. 2, pp. 173–176, Jan. 2019, doi: 10.1109/LPT.2018.2888806.

[15] D. F. Siriani et al., "Mode control in photonic crystal vertical-cavity surface-emitting lasers and coherent arrays," *IEEE J. Sel. Topics Quantum Electron.*, vol. 15, no. 3, pp. 909–917, May/Jun. 2009, doi: 10.1109/JSTQE.2008.2012121.

[16] Z. Gao, S. T. M. Fryslie, B. J. Thompson, P. S. Carney, and K. D. Choquette, "Parity-time symmetry in coherently coupled vertical cavity laser arrays," *Optica*, vol. 4, no. 3, Mar. 2017, Art. no. 323, doi: 10.1364/OPTICA.4.000323.

[17] Z. Gao, B. J. Thompson, H. Dave, and K. D. Choquette, "The complex coupling coefficient of coherent VCSEL arrays," in *Proc. IEEE Int. Semicond. Laser Conf.*, 2018, pp. 1–2. doi: 10.1109/ISLC.2018.8516184.

[18] P. Strzebonski and K. Choquette, "Complex waveguide supermode analysis of coherently-coupled microcavity laser arrays," *IEEE J. Select. Topics Quantum Electron.*, vol. 28, no. 1, Jan./Feb 2022, Art. no. 1700306, doi: 10.1109/JSTQE.2021.3096167.

[19] P. Strzebonski, "Advances in semiconductor laser mode and beam engineering," Thesis dissertation, Univ. of Illinois at Urbana-Champaign, 2021.

[20] S. T. M. Fryslie, M. T. Johnson, and K. D. Choquette, "Coherence tuning in optically coupled phased vertical cavity laser arrays," *IEEE J. Quantum Electron.*, vol. 51, no. 11, Nov. 2015, Art. no. 2600206, doi: 10.1109/JQE.2015.2481724.

[21] D. F. Siriani and K. D. Choquette, "Implant defined anti-guided vertical-cavity surface-emitting laser arrays," *IEEE J. Quantum Electron.*, vol. 47, no. 2, pp. 160–164, Feb. 2011, doi: 10.1109/JQE.2010.2068278.

[22] W. North, N. Jahan, P. Strzebonski, and K. D. Choquette, "Modal characteristics of coupled vertical cavity surface emitting laser diode arrays," *J. Appl. Phys.*, vol. 132, no. 17, Nov. 2022, Art. no. 173102, doi: 10.1063/5.0119912.

[23] D. F. Siriani, K. D. Choquette, and P. S. Carney, "Stochastic coupled mode theory for partially coherent laser arrays," *J. Opt. Soc. Amer. A*, vol. 27, no. 3, Mar. 2010, Art. no. 501, doi: 10.1364/JOSAA.27.000501.

[24] Z. Gao, M. T. Johnson, and K. D. Choquette, "Rate equation analysis and non-hermiticity in coupled semiconductor laser arrays," *J. Appl. Phys.*, vol. 123, no. 17, May 2018, Art. no. 173102, doi: 10.1063/1.5022044.

[25] Z. Gao, B. J. Thompson, H. Dave, S. T. M. Fryslie, and K. D. Choquette, "Non-hermiticity and exceptional points in coherently coupled vertical cavity laser diode arrays," *Appl. Phys. Lett.*, vol. 114, no. 6, Feb. 2019, Art. no. 061103, doi: 10.1063/1.5083084.

[26] B. J. Thompson, Z. Gao, S. T. M. Fryslie, and K. D. Choquette, "Mode engineering in linear coherently coupled vertical-cavity surface-emitting laser arrays," *IEEE J. Select. Topics Quantum Electron.*, vol. 25, no. 6, Nov./Dec. 2019, Art. no. 1701205, doi: 10.1109/JSTQE.2019.2950799.

[27] L. A. Coldren, S. W. Corzine, and M. L. Mašanović, *Diode Lasers and Photonic Integrated Circuits: Coldren/Diode Lasers 2E*. Hoboken, NJ, USA: Wiley, 2012. doi: 10.1002/9781118148167.

[28] N. Jahan, W. North, P. Strzebonski, and K. D. Choquette, "Supermode switching in coherently-coupled vertical cavity surface emitting laser diode arrays," *IEEE J. Sel. Topics Quantum Electron.*, vol. 28, no. 1, Jan. 2022, Art. no. 1700505, doi: 10.1109/JSTQE.2021.3117236.

[29] P. Strzebonski, W. North, and K. D. Choquette, "Fourier-method beam analysis for coherent vertical cavity surface emitting laser arrays," *J. Opt. Soc. Amer. A, JOSAA*, vol. 39, no. 4, pp. 563–570, Apr. 2022, doi: 10.1364/JOSAA.446584.

[30] W. North and K. D. Choquette, "Supermode evolution in dual element coupled VCSEL arrays," in *Proc. Conf. Lasers Electro-Opt.*, 2023, Art. no. STh4Q.3.